

Evaluation of GM-APD array devices for low-light-level imaging

Kimberly Kolb, Brandon Hanold, Joong Lee, Donald F. Figer

Center for Detectors, Rochester Institute of Technology, 74 Lomb Memorial Drive, Rochester, NY, USA 14586

ABSTRACT

The ability to count single photons is necessary to achieve many important science objectives in the near future. This paper presents the lab-tested performance of a photon-counting array-based Geiger-mode avalanche photodiode (GM-APD) device in the context of low-light-level imaging. Testing results include dark count rate, afterpulsing probability, intra-pixel sensitivity, and photon detection efficiency, and the effects of radiation damage on detector performance. The GM-APD detector is compared to the state-of-the-art performance of other established detectors using Signal-to-noise ratio as the overall evaluation metric.

Keywords: GM-APD, photon counting, imaging detectors, low-light-level imaging, signal-to-noise ratio

1. INTRODUCTION

Single photon counting detectors have the potential to be the next big advancement for low-light-level imaging. The ability to count single photons is necessary to achieve many important science objectives in the near future. A good example is the discovery of exoplanets, which requires advancements in detector performance, especially in the case of direct imaging. A reasonable estimate for the signal in such a scenario is a 30 mag object (an Earth-like planet orbiting a Sun-like star 10 pc away, a signal of 0.1 photons/s/pixel). To reach a signal-to-noise ratio (SNR) of 1 in this scenario, a detector with state-of-the-art read noise ($3 e^-$) would need an exposure time of roughly 1100 s with 70% Quantum Efficiency (QE). A photon counting detector would need only 450 s at the same QE (a 2.4x reduction).

1.1 GM-APD Device Architecture

One approach to a zero read noise, photon-counting detector is the GM-APD imaging array presented here. Historically, GM-APDs have been used for temporal measurements in applications such as LIDAR^{1,2} and adaptive optics systems³, as well as a replacement for photo-multiplier tubes.⁴ By operating a GM-APD detector in photon-counting mode, where each pixel returns a digital signal, zero read noise can be achieved. In the device discussed in this paper, each pixel is made up of three distinct regions with specific functions. Figure 1 shows the internal structure of a single pixel.

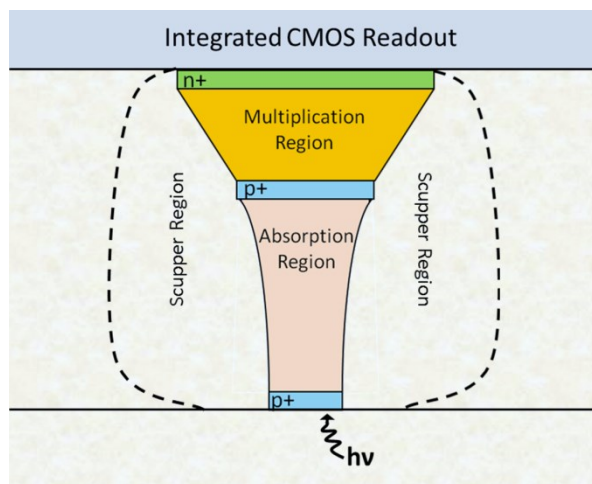


Figure 1 This figure shows the GM-APD design for one pixel (not to scale).

The absorption region has a medium-strength electric field that moves carriers to the multiplication region, which has a strong electric field to facilitate avalanches. A weak electric field region, called a “scupper,” surrounds the absorption

and multiplication regions of each pixel to direct carriers generated outside of these regions to the cathode without initiating an avalanche, reducing the dark count rate.³

1.2 GM-APD Array Operation

Semiconductor-based photon counting detectors use avalanche multiplication to amplify the signal. Avalanche multiplication occurs when a free carrier encounters a strong electric field. The carrier is accelerated by the electric field and may excite another carrier into the conduction band through impact ionization. The strong electric field then accelerates both carriers, which may go on to excite other carriers. This process continues as long as the carriers remain in a high field region, resulting in amplification of the original signal.

For the GM-APD device presented here, the exposure time is accumulated over a series of detection periods. Each detection period contains a user-defined gate time (t_{gate}) and hold-off time (t_{ho}). t_{gate} is the period during which a pixel can avalanche, and t_{ho} is the period between gates. The exposure time is t_{gate} multiplied by the number of gates.

At the beginning of a gate, a short ($\sim 0.1 \mu\text{s}$) arm pulse is asserted to increase the bias above the breakdown voltage. If an avalanche occurs during a gate, the bias is decreased below breakdown to quench the avalanche. Only one avalanche can be recorded per gate because the pixel cannot avalanche after the voltage is decreased. At the end of the gate, the state of the pixel is recorded (a 1 or a 0, where a 1 means that an avalanche occurred during the gate), and then a short ($\sim 0.1 \mu\text{s}$) disarm pulse is asserted to decrease the bias below the breakdown voltage for all pixels that did not avalanche during the gate. This ensures that no avalanches occur during the hold-off time, which immediately follows the previous gate and lasts until the beginning of the next gate. The output from the detectors is the total number of ones for each pixel.

2. DEVICE CHARACTERIZATION

The GM-APD device characterization presented here includes dark count rate (DCR), afterpulsing probability (P_{aft}), intra-pixel sensitivity (IPS), and photon detection efficiency (PDE) (crosstalk for these devices is negligible, $< 1\%$). The radiation experiment is discussed and its effects on detector performance are presented.

2.1 Dark Count Rate

DCR is the rate of counts generated in the absence of light. In this report, DCR is corrected for dead time and the experiments to measure it are designed to minimize counts from afterpulsing. As such, the DCR is expressed as electrons/s/pixel (Hz). Figure 2 shows the pre-radiation DCR results for the GM-APD device.

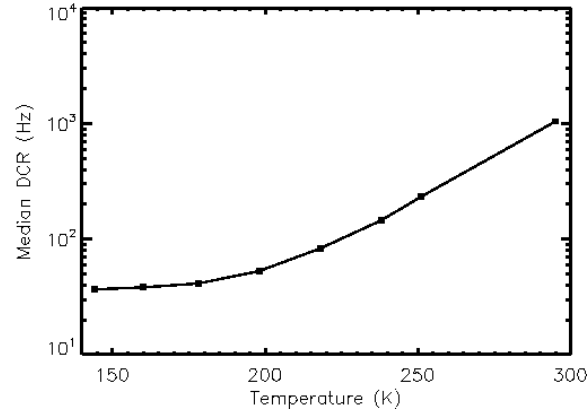


Figure 2. This plot shows median DCR vs temperature for a GM-APD device.

2.2 Afterpulsing

Afterpulsing is an increase in count rate following an avalanche in the same pixel. Afterpulsing is often caused by traps, which are energy states that exist only around material defects in the detector substrate. Instead of being collected, charge becomes “trapped” in these energy states and is released a random amount of time later. Afterpulsing increases the measured DCR and decreases the SNR. Afterpulsing probability (P_{aft}) can be measured experimentally by observing individual gates^{5, 6}, but the operation of these devices is not conducive to that method. Here, P_{aft} is calculated by comparing measured DCR at various hold-off times. Figure 3 shows P_{aft} vs t_{ho} , before irradiation. The minimum t_{ho} required to avoid afterpulsing was 1 ms for temperatures below 170 K and 10 μs for warmer temperatures.

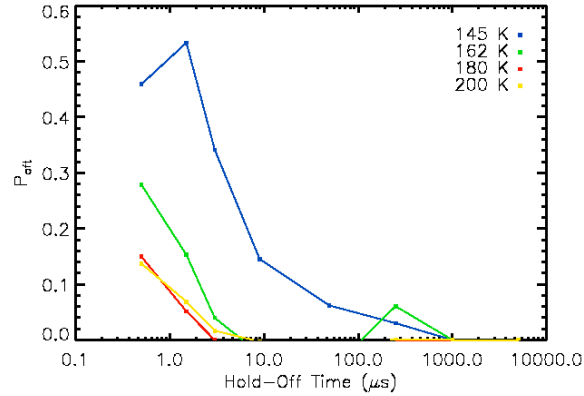


Figure 3. Median afterpulsing probability vs hold-off time is shown for various temperatures.

2.3 Intra-Pixel Sensitivity

IPS is the photon detection efficiency as a function of location inside a pixel. Ideally, the IPS function would be 1 across the entire pixel, but for the GM-APDs tested, the active area is concentrated at the center of each pixel and can be modeled as a 2D Gaussian function. IPS was measured by projecting a small pinhole image onto the detectors with a FWHM (the full width of the Gaussian curve at half of the maximum) of $3.8 \mu\text{m}$. The spot was moved through a 2×2 pixel grid of $2.5 \mu\text{m}$ steps, with an exposure at each grid location. The measured IPS function was de-convolved with the expected laser spot size to calculate the actual IPS function of the pixel, which was used to calculate fill factor and FWHM.

Figure 4 shows the measured IPS of a representative pixel on one detector. Note that the scan area is 2×2 pixels, but the plot shows the signal from only one pixel. The pre-radiation FWHM was $10.2 \mu\text{m} \pm 5 \mu\text{m}$. The size of the laser spot is highly dependent on the focus, so it is likely that the variance in FWHM is a function of the variance of the spot size when moving the spot projector and re-focusing. The mean pre-radiation fill-factor, the percent of the pixel area that is active, was 18.7%.

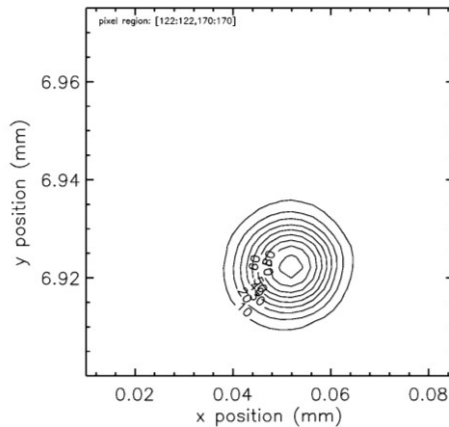


Figure 4. Sample IPS results from pixels on a GM-APD detector are shown. The center of the pixel is inside the central contour. These results are not corrected for laser spot size.

2.4 Photon Detection Efficiency

PDE is the inferred photo-generation rate divided by the incident photon rate. The GM-APD data presented here is for a LFF architecture, which limits PDE to values below 1%. This performance is not representative of what is expected for detectors optimized for imaging applications. Additionally, the PDE was measured at a moderate overbias (2 V) to limit DCR – at twice the overbias (4 V) the PDE is nearly 50% higher.

The detector replacement method was used to determine the ratio of photon flux measured by the calibrated photodiode in the integrating sphere to the photon flux incident on the detector. In this method, the detector is replaced by a second calibrated photodiode during the experiment. The results were used to calculate the flux at the detectors based on the

diode readings inside the integrating sphere. For each new wavelength setting, the mechanical parts of the monochromator move, which causes the background light level to change at each wavelength. Therefore, dark exposures were taken at each wavelength setting to account for these changes. The dark signal was subtracted from the total signal to calculate the photo-generated signal.

Figure 5 shows the median PDE of a GM-APD device for a range of wavelengths at 130 K. The short-wavelength cutoff was ~ 480 nm and the peak PDE, $0.26\% \pm 0.03\%$, occurred at 730 nm. The PDE presented in Figure 5 is not corrected for fill factor, and is actually the mean sensitivity over the entire pixel. The measured PDE would be higher if the signal were concentrated in the center of the pixels (e.g., by microlenses²). The IPS function and the measured PDE were used to calculate the sensitivity at the center of the pixel. The pre- and post-radiation peak sensitivity at 730 nm were 1.2% and 0.7%, based on the IPS function in section 2.3.

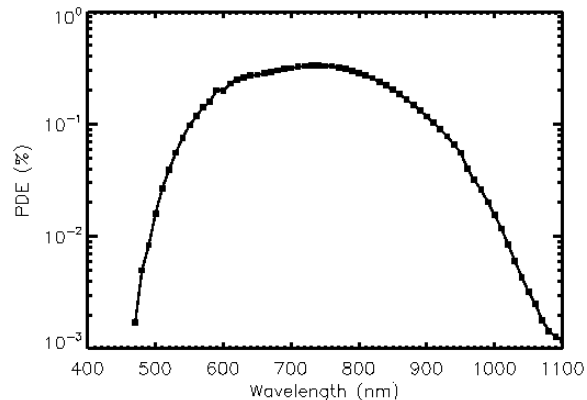


Figure 5. This figure shows median PDE (%) vs wavelength for a GM-APD detector.

2.5 Radiation Testing

Three GM-APD devices were irradiated at Massachusetts General Hospital's Francis H. Burr Proton Therapy Laboratory with monoenergetic 60 MeV protons. They were exposed to a cumulative dose of 50 krad (Si) in geometrically spaced doses, simulating 10 solar cycles at an L2 orbit (assuming a 1 cm Al shield). The entire testing system was transported and set up at the proton beam facility so that the detectors could be tested between radiation doses in a vacuum- and temperature-controlled environment. The system was set up so that the detectors were in the beam path inside the dewar, with the radiation passing through a thin metal cover, which kept the dewar completely dark.

The breakdown voltage of the device increased by 1.5 V after irradiation. As atoms in the silicon lattice become displaced by radiation damage, the resistivity of the bulk material increases.⁷ The applied voltage in a GM-APD is divided between the multiplication and absorption regions (see Figure 1). If the resistance of the absorption region significantly increases after irradiation, less of the applied voltage falls across the multiplication region and more applied voltage is required to achieve the electric field necessary for breakdown. DCR increased significantly at temperatures above 200 K, by an average of $\sim 2x$, but decreased slightly at colder temperatures due to the shift in breakdown voltage. The PDE also decreased to $0.18\% \pm 0.002\%$ after irradiation, though there was no statistical difference between pre- and post-radiation IPS functions or fill factor. P_{aft} increased at all temperatures after irradiation, and a new trend emerged in which P_{aft} increased with temperature above 200 K instead of continuing to decrease. The minimum t_{ho} required to avoid afterpulsing was 1 ms below 200 K and 5 ms for warmer temperatures, which negatively affected the duty cycle of the device.

3. LOW-LIGHT-LEVEL IMAGING APPLICATIONS

The absence of read noise for a GM-APD detector operated in photon-counting mode makes the detectors a promising alternative to CCDs and CMOS detectors in low-light-level imaging applications. The benefit of zero read noise is especially valuable in fast exposure scenarios, such as astronomical imaging of pulsars and stellar flares⁸, transit photometry of exoplanets⁹, adaptive optics³, LIDAR imaging^{10, 2}, or biological imaging of tumors¹¹ and the brain.¹² In short exposures that require fast readout rates (e.g., MHz pixel rates), read noise in CCD and CMOS detectors can approach 10-100 electrons rms¹³. Long exposure applications, such as direct imaging of faint objects, also benefit from zero read noise, though the advantage over existing technology is less significant. For long integration times, the readout

rate can be much slower, and read noise for CMOS and CCD detectors falls to a few electrons rms.^{13, 14, 15} While EMCCDs in photon-counting mode operate in a way that makes read noise negligible regardless of the readout rate¹⁶, signal loss due to thresholding is a concern due to uncertainty in the gain. Therefore, comparison between GM-APDs and other imaging detector types is necessary to understand the role they may play in future imaging applications. The performance of each detector will be evaluated for fast exposures (0.1 s wall time) and long exposures (1000 s wall time). Wall time is the total time required to take an image, and includes the exposure time as well as the readout time.

3.1 First Generation Performance

Detector performance after 1 solar cycle, 5 krad (Si), and 10 solar cycles, 50 krad (Si), is modeled based on in-situ and post-radiation measurements. In order to interpolate the characteristics for 1 solar cycle of radiation (11 years), the effects of radiation on breakdown voltage are assumed to be linear and the relative trend in DCR is assumed to be the same as in pre-radiation measurements. For all simulations, $t_{gate} = 300 \mu s$ and $\lambda = 730 \text{ nm}$. The duty cycle is calculated by assuming that t_{ho} is the minimum required to avoid afterpulsing.

Table 1. SNR modeling characteristics for a GM-APD device at various radiation levels are shown.

Parameter	Pre-Radiation Value	1 solar cycle	10 solar cycles
DCR (Hz)	38.21	50.70	17.40
PDE (%)	0.26	0.25	0.18
Duty Cycle (%)	96.8	96.8	85.7
Optimum Operating Temperature (K)	160	160	140

The effective overbias for the post-radiation data after 10 solar cycles is 0.5 V, which is why the DCR is lower than for the other two radiation levels. For reference, at the same temperature and overbias, the pre-radiation DCR was 5.9 Hz, implying an increase of 11.5 Hz after 10 solar cycles of radiation at 140 K. Figure 6 shows the expected SNR for pre- and post-radiation performance characteristics.

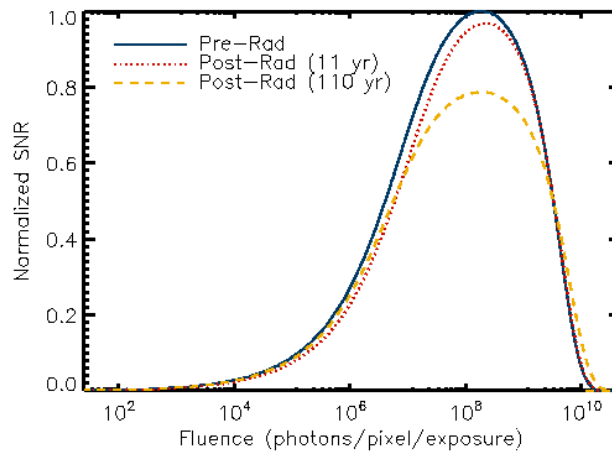


Figure 6. This figure shows pre- and post-radiation SNR of a GM-APD for a 1000 s (wall time) exposure. The SNR is normalized to the maximum SNR before irradiation.

3.2 Suggested Improvements

Although the first-generation devices had significant noise and very low efficiency, a few simple, targeted improvements would greatly improve their performance. As alluded to in section 2.4, a microlens array would greatly improve PDE by focusing incident photons in the center of the pixel. However, re-designing the internal device structure would lead to the most significant gains in performance.

As designed, the scupper region in Figure 1 mitigates DCR at the expense of efficiency. Even carriers generated by photons in the absorption region have a significant probability of moving to the scupper region. However, the scupper would no longer be necessary if the dark current were not so high. The high dark current in these devices is due to a number of factors, including damage introduced by thinning the detector. Current state-of-the-art silicon detectors have

dark current on the order of 8 e-/s at room temperature¹⁷, achieved through various processing and design improvements. Improving the dark current would eliminate the need for the scupper region and allow the efficiency to increase to the levels seen in other GM-APD devices, near 80%.¹⁸ Increasing the quality of the substrate will also lead to a decrease in afterpulsing. Ideally, there should be no traps, and therefore no afterpulsing, in a majority of the pixels.

Care should be taken to keep the volume of the multiplication region as small as possible. Increased volume leads to more carriers participating in each avalanche. This increases optical crosstalk between pixels, which has been measured in devices that have large multiplication regions. Significant optical crosstalk leads to large groups of pixels firing during a single gate, which makes signal estimation nearly impossible. In order to mitigate the effects of a larger multiplication area, which must occur if the active area is expanded, optical isolation trenches should be added between pixels.

3.3 Projected Performance and Comparison to Current Technology

In order to assess the performance of GM-APD array imagers for future applications, they must be compared to current state-of-the-art semiconductor-based technologies, including standard CCDs^{13, 15}, CMOS detectors¹⁴, low-light-level CCDs (L3CCDs)¹³, and EMCCDs.¹⁶ Table 2 shows reasonable best-performance metrics for each established detector, and projected performance for a next-generation GM-APD.

Table 2. This table shows state-of-the-art performance characteristics for fast exposures of 0.1 s (requiring pixel rates in the tens of MHz range for moderately-sized CCD- and CMOS-based imagers) and long exposures of 1000 s.

Parameter	Standard CCD		CMOS APS		L3CCD		EMCCD		GM-APD	
	0.1 s	1000 s	0.1 s	1000 s	0.1 s	1000 s	0.1 s	1000 s	0.1 s ($t_{gate} = 210 \mu s$)	1000 s ($t_{gate} = 1 ms$)
Dark Current (e-/s/pix)	0.00021	0.00021	0.015	0.015	0.00021	0.00021	0.00021	0.00021	0.027	0.027
CIC (e-/pix/frame)	0	0	0	0	0.0025	0	0.0025	0	0	0
Read Noise (e- rms)	10	2	10	3	<<1	<<1	<<1	<<1	0	0
QE	90%	90%	90%	90%	90%	90%	90%	90%	70%	70%
Duty Cycle	90%	100%	90%	100%	90%	100%	9%	100%	100%	100%
ADC Saturation (1000s e-)	72	72	100	100	1,000	1,000	1,000	1,000	N/A	N/A

The gate time for the GM-APD is set to the minimum time required to read out the array for the fast (0.1 s) exposure. By doing this, the entire array can be read out during the next gate and the duty cycle can be 100% (assuming that there is no afterpulsing in most of the pixels). The 1 ms gate time for the long exposure is to maximize SNR at low fluence. The projected DCR is a scaled version of the state-of-the-art DCR reported in section 3.2, based on the pre-radiation DCR trend presented in Figure 2. Figure 7 shows the expected SNR for each device in Table 2 for both imaging scenarios.

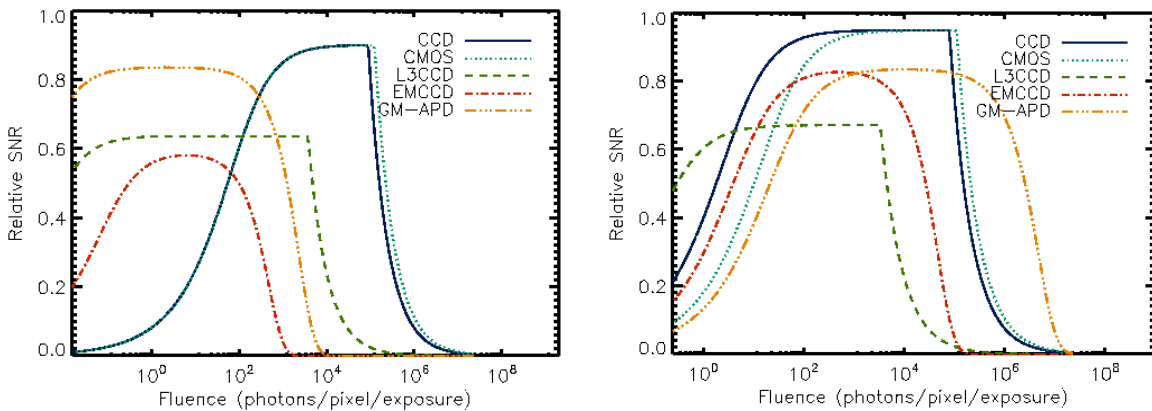


Figure 7. This plot shows the relative SNR for a variety of detector technologies in two imaging scenarios. On the left, a fast exposure of 0.1 s wall time is simulated. On the right, a long exposure of 1000 s wall time is simulated. The SNR for each device is normalized to the shot noise limit for each fluence value.

The CCD and CMOS detectors have nearly the same performance except for a small change in ADC saturation. Their poor performance at low fluence levels in the fast exposure scenario is due to the high read noise necessary to read out the array quickly. This disadvantage does not apply for long exposures where the read noise decreases significantly. The L3CCD is limited to 70% of the shot-noise-limited SNR because of the excess noise factor (ENF) caused by uncertainty in the gain. It also saturates more quickly, even though its ADC has a higher saturation level than the CCD or CMOS devices, because of the gain. The EMCCD suffers from very low duty cycle in the fast exposure scenario due to the maximum pixel readout rate (tens of MHz). Additionally, the clock-induced-charge (CIC), which introduces as much noise as an equivalent amount of dark current, is high when the pixel readout rate is as high as required here. In the fast exposure scenario, the GM-APD clearly dominates at fluence levels between 1 and 100 photons (corresponding to 10-1000 photons/s in this simulation). If t_{gate} were shorter (e.g., if the readout electronics were optimized for fast readout), the detector would saturate later and offer significant competition to the CCD and CMOS detectors at higher fluence levels. The absence of read noise for the GM-APD, even though the dark current is higher, makes it the best candidate for fast imaging if the projected performance levels can be met. For long exposures, the higher dark current of the GM-APD results poor performance below a total fluence of ~ 100 photons (0.1 photons/s), and it is out-performed by the CCD and CMOS devices between 1,000 and 100,000 photons (1-100 photons/s). However, if DCR were to improve to the levels of CCD and CMOS devices, the GM-APD would out-perform the EMCCD and the L3CCD at all fluence levels, and the CCD and CMOS devices below 10 photons (0.01 photons/s).

3.4 Radiation Tolerance

CCD- and CMOS-based detectors experience increases in dark current after radiation damage from two main sources: bulk damage and ionization effects.¹⁹ The latter source is caused by damage at the surface of the devices at the silicon/insulator interface. In GM-APDs, this type of damage does not affect the DCR because the avalanche initiation probability for carriers generated at the surface of the device is effectively zero. The bulk damage is mostly comprised of deep-level defects (lattice displacement), which act as generation / recombination centers in the material. Carrier generation at deep-level defect sites requires thermal energy, and is very sensitive to changes in temperature – the generated current increases exponentially with temperature.

At 160 K, the increase in DCR after one solar cycle (11 years) was 12.5 e-/s/pix. In contrast, an x-ray detection CCD device on board the ASCA satellite (with similar shielding) experienced an increase of 0.8 e-/s/pix/yr, which would extrapolate to an increase of 8.8 e-/s/pix after one solar cycle (a rate of increase of 1.8 e-/s/pix/krad(Si), assuming that the measurement window was representative of the flux distribution for the entire solar cycle).²⁰ While the CCD experience less radiation damage, the GM-APD is not susceptible to surface-generated dark current, which gives it the potential to surpass the CCD's radiation tolerance with some design improvements. In addition to an increase in dark current, however, the CTE for CCD-based devices decreases significantly after irradiation.^{21, 22} These radiation effects are common to standard CCDs, L3CCDs, and EMCCDs since they all utilize the same basic structure and operation. It should be noted that increased shielding, such as on the STIS instrument on the Hubble Space Telescope, can significantly decrease the radiation dose per year and the radiation-induced dark current.²³

4. CONCLUSIONS

GM-APDs are a promising technology for low-light-level imaging applications. While the first-generation performance is not ideal, targeted improvements can be made that would increase the performance of next-generation devices to be competitive with state-of-the-art CCD- and CMOS-based imaging detectors. They offer a potential, though currently unrealized, advantage in radiation tolerance over other types of detectors, as well. With targeted design improvements, these detectors will make impressive candidates for both ground- and space-based imaging applications that require fast exposures.

REFERENCES

- [1] Yuan, P. et al., "32 x 32 Geiger-mode LADAR Cameras," Proc. of SPIE 7648, 76840C (2010).
- [2] Itzler, M. A. et al., "Design and performance of single photon APD focal plane arrays for 3-D LADAR imaging," Proc. of SPIE 7780, 77801M (2010).

- [3] Aull, B. F., Schuette, D. R., Reich, R. K. and Johnson, R. L., "Adaptive optics wavefront sensors based on photon-counting detector arrays," Proc. of SPIE 7736, 773610 (2010).
- [4] Renker, D., "Geiger-mode avalanche photodiodes, history, properties, and problems," Nuclear Instruments & Methods in Physics Research Section A 567(1), 48-56 (2006).
- [5] Itzler, M. A., Jiang, X. and Entwistle, M., "Power law temporal dependence of InGaAs/InP SPAD afterpulsing," Journal of Modern Optics 59(17), 1472-1480 (2012).
- [6] Jensen, K. E., Hopmah, P. I., Duerr, E. K., Dauler, E. A. and Donnelly, J. P., "Afterpulsing in Geiger-mode avalanche photodiodes for 1.06um wavelength," Applied Physics Letters 88(13), 133503 (2006).
- [7] Li, Z., "Radiation Hardness/Tolerance of Si Sensors/Detectors for Nuclear and High Energy Physics Experiments," Proc. of Pixel 2002, (2002).
- [8] Mackay, C., Weller, K. and Suess, F., "Photon Counting EMCCDs: New Opportunities for High Time Resolution Astrophysics," Proc. of SPIE 8453, 845302 (2012).
- [9] Borucki, W. J. et al., "Kepler Planet-Detection Mission: Introduction and First Results," Science 327(5968), 977-980 (2010).
- [10] Albota, M. A. et al., "Three-Dimensional Imaging Laser Radars with Geiger-Mode Avalanche Photodiode Arrays," Lincoln Laboratory Journal 13(2), 351-370 (2002).
- [11] Weissleder, R., Tung, C.-H., Mahmood, U. and Bogdanov Jr., A., "In vivo imaging of tumors with protease-activated near-infrared fluorescent probes," Nature Biotechnology 17(4), 375-378 (1999).
- [12] Hillman, E. M. C., "Optical brain imaging in vivo: techniques and applications from animal to man," Journal of Biomedical Optics 12(5), 051402 (2007).
- [13] Basden, A. G., Haniff, C. A. and Mackay, C. D., "Photon counting strategies with low-light-level CCDs," Monthly Notices of the Royal Astronomical Society 345(3), 985-991 (2003).
- [14] Bai, Y. et al., "Hybrid CMOS Focal Plane Array with Extended UV and NIR Response for Space Applications," Proc. of SPIE 5167, 83-93 (2004).
- [15] Gilliland, R. L., Rajan, A. and Deustua, S., "WFC3 UVIS Full Well Depths, and Linearity Near and Beyond Saturation," Space Telescope WFC3 Instrument Science Report 2010(10), 1-21 (2010).
- [16] Daigle, O., Djazovski, O., Laurin, D., Doyon, R. and Artigau, E., "Characterization results of EMCCDs for extreme low light imaging," Proc. of SPIE 8453, 845303 (2012).
- [17] Jackson, J. C., Morrison, A. P., Phelan, D. and Mathewson, A., "A Novel Silicon Geiger-Mode Avalanche Photodiode," Proc. of IEDM 32, 797-800 (2002).
- [18] Renker, D. and Lorenz, E., "Advances in solid state photon detectors," Journal of Instrumentation 4(4), P04004 (2009).
- [19] Janesick, J., Elliott, T. and Pool, F., "Radiation Damage in Scientific Charge-Coupled Devices," IEEE Transactions on Nuclear Science 36(1), 572-578 (1989).
- [20] Yamashita, A. et al., "Radiation Damage to Charge Coupled Devices in the Space Environment," IEEE Transactions on Nuclear Science 44(3), 847-853 (1997).
- [21] Mori, K. et al., "Proton radiation damage experiment on P-Channel CCD for an X-ray CCD camera onboard the ASTRO-H satellite," Nuclear Instruments and Methods in Physics Research A 731, 160-165 (2013).
- [22] Janesick, J., Soli, G., Elliott, T. and Collins, S., "The Effects of Proton Damage on Charge-Coupled Devices," Proc. of SPIE 1447, 87-108 (1991).
- [23] Kimble, R. A., Goudfrooij, P. and Gilliland, R. L., "Radiation damage effects on the CCD detector of the Space Telescope Imaging Spectrograph," Proc. of SPIE 4013, 532-544 (2000).